RESEARCH ARTICLE

**ADVANCED
ENERGY & SUSTAINABILITY
RESEARCH**
Open Access

www.advenergysustres.com

Stable and Dendrite-Free Lithium Metal Anodes Enabled by Ionic/Electronic Li₂S/Mo Interlayer

Lishuang Fan, Zhikun Guo, Dan Zhao, Chenyang Zhao, Xingyuan Lu, Aosai Chen, Xiaoju Yin, Yu Zhang, Bing Sun,* and Naiqing Zhang*

The wide applications of high-capacity lithium metal anodes for lithium metal batteries are restricted by the uncontrollable lithium dendrite growth caused by the uneven lithium deposition and the infinite volume change of lithium anodes during the plating/stripping process. Herein, the composite ionic/electronic interlayer of Li₂S/Mo is deposited on the surface of stainless steel mesh (SSM) by in situ electrochemical conversion reaction from MoS₂ nanosheet arrays. The Li₂S/Mo interlayer with high ionic conductivity can regulate uniform lithium-ion flux and promote homogeneous lithium deposition without dendrite growth. The half cells with Li₂S/Mo-modified SSM current collector show stable cycling performance of more than 400 cycles at 1 and 1 mAh cm⁻², with the average Coulombic efficiency higher than 96%. By coupling with LiFePO₄ cathodes, the assembled full cells demonstrate improved cycling performance. This work provides a new idea for using metal sulfides as a lithiophilic interlayer to facilitate dendrite-free lithium deposition.

L. Fan, Z. Guo, D. Zhao, C. Zhao, X. Lu, A. Chen, X. Yin, Y. Zhang, N. Zhang
State Key Laboratory of Urban Water Resource and Environment
School of Chemistry and Chemical Engineering
Harbin Institute of Technology
Harbin, China
E-mail: zhangnq@hit.edu.cn

L. Fan, X. Yin, N. Zhang
Academy of Fundamental and Interdisciplinary Sciences
Harbin Institute of Technology
Harbin 150001, China

B. Sun
Centre for Clean Energy Technology
School of Mathematical and Physical Sciences
Faculty of Science
University of Technology Sydney
Broadway, Sydney, NSW 2007, Australia
E-mail: bing.sun@uts.edu.au

The ORCID identification number(s) for the author(s) of this article can be found under https://doi.org/10.1002/aesr.202100051.

1. Introduction

To meet the stringent requirements of our modern society for high-energy-density energy-storage devices, the development of advanced and reliable rechargeable battery systems is imminent.[1–4] Recently, lithium−sulfur and lithium−oxygen batteries directly using lithium metal as the anode showed great potential.[5–8] The theoretical specific capacity of lithium metal is 3860 mAh g⁻¹, and the electrochemical potential is −3.040 V versus standard hydrogen electrode, which demonstrates high expectations for the researchers.[9,10] Unfortunately, the application of lithium anodes is seriously hindered by the following reasons.[11–13] First, the uneven deposition of lithium and the breakage of solid−electrolyte interphase (SEI) lead to the formation of dendrites, which can cause short circuit and even more severe safety problems. In addition, the formation of "dead lithium" on the surface of lithium metal anodes during the process of repeated deposition/stripping of lithium ion/lithium reduces the use rate of active materials. Furthermore, the infinite volume expansion and electrode comminution lead to sharp attenuation of cycle life.

So far, researchers have explored a variety of approaches to inhibit dendrite formation and volume changes, including optimizing current liquid electrolytes, modifying separators, exploring solid or polymer electrolytes, designing artificial protective interfaces, and constructing appropriate current collectors.[14–31] The initial nucleation and deposition behaviors of lithium show important influence on the subsequent deposition. An important way to achieve homogeneous lithium deposition is to improve the chemical affinity between the substrate and deposited lithium.[32] Zhang et al. introduced nitrogen-containing functional groups to graphene nanosheets and preferentially deposited lithium at the nitrogen doping sites to facilitate homogenous lithium deposition.[9] Liang and coworkers improved the surface lithiophilicity of the conductive substrate by in situ modification of Co₃O₄ nanosheets arrays on the surface of nickel foam.[33] Cao and coworkers constructed NiFₓ nanosheets on Ni foam via in situ decomposition of polytetrafluoroethylene (PTEF) coating layer at high temperature.[34] The lithiophilic NiFₓ interlayer greatly reduced the nucleation barrier, which facilitates homogenous lithium nucleation and deposition. Meanwhile, the reaction between NiFₓ and lithium ions formed an LiF-enriched SEI layer, which enhanced

the interfacial stability between lithium metal anodes and liquid electrolytes. Although these studies have achieved some good results, the excessive deposition at scattered nucleation points still induces the formation of lithium dendrites. How to generate homogeneously distributed nucleation sites and facilitate the rapid migration of lithium ions to the nucleation sites remain the biggest challenge to achieve dendrite-free lithium metal anodes.

Herein, we first deposit MoS_2 nanosheets on the surface of the stainless steel mesh (SSM) and then transfer them into uniform Li_2S/Mo microarrays via the electrochemical conversion reaction. The SSM with a regular network structure has high mechanical strength and excellent electronic conductivity, which is conducive to rapid electron transportation and fast deposition dynamics. The interlayer composed of Li_2S/Mo can effectively regulate lithium nucleation and deposition behaviors. A large number of uniformly distributed Mo atoms possess high electrical conductivity and good lithiophilicity, providing low-overpotential deposition sites for lithium. Meanwhile, Li_2S has high ionic conductivity, which enables lithium ions to migrate rapidly to the nucleation sites on the surface of the nanosheets. Based on the earlier unique design, Li_2S/Mo-modified SSM can well regulate the deposition behavior of lithium metal, achieving dendrite-free lithium metal anodes.
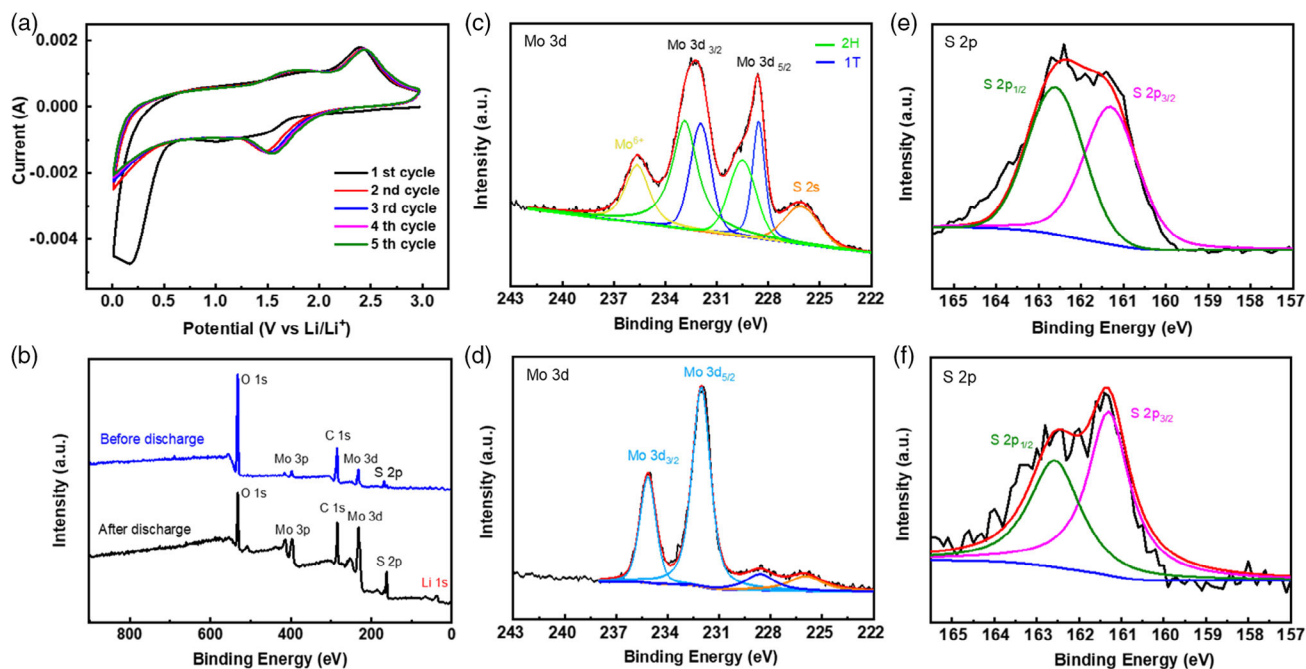
2. Results and Discussion

The schematic diagrams of Li deposition behaviors on pristine SSM and MoS_2-coated SSM (MoS_2@SSM) substrates are shown in **Figure 1**a,b. Li dendrites are easily formed when directly deposited on the surface of the SSM. While uniform Li

deposition can be achieved on the MoS_2@SSM substrate, the surface of pristine SSM is smooth (Figure S1, Supporting Information). After hydrothermal treatment, the surface of SSM is uniformly covered by MoS_2 nanosheets, which can be confirmed by X-ray diffraction (XRD) (Figure 1c). The characteristic peaks of the SSM are located at 43.6°, 50.8°, and 74.7°. For MoS_2@SSM substrate, there are three obvious characteristic peaks at 8.8°, 17.8°, and 32.5°, corresponding to (002) plane, (004) plane, and (100) plane of MoS_2, respectively.[35] The lamellar structure of MoS_2 is conducive to the insertion of Li ions, providing abundant reaction sites and facilitating further conversion reaction. The nanosheets grown on SSM are uniform and closely aligned (Figure 1d,e). The small cavities surrounding the arrays and the periodic network structure of the SSM provide a spatial constraint for Li deposition. The thickness of the MoS_2 layer is about 1 μm, and some nanochannels can be observed from the cross-section scanning electron microscopy (SEM) image in Figure S2, Supporting Information.

To reveal the electrochemical behavior of Li-ion intercalation in MoS_2 nanosheets, cyclic voltammetry (CV) measurements were carried out on the cells with SSM and MoS_2@SSM substrates in the ether-based electrolyte (1 M LiTFSI in DOL/DME 1:1). As shown in the CV curves of the cell with SSM substrate in Figure S3, Supporting Information, there are no obvious oxidation/reduction reactions between the SSM substrate and Li ions. **Figure 2**a shows the CV curves of the cell with MoS_2@SSM substrates. In the first cathodic process, two reduction peaks appeared, the peak at 0.94 V belongs to Li-ion insertion in MoS_2, forming Li_xMoS_2, and the peak at 0.19 V belongs to Li_xMoS_2 conversion into Li_2S and Mo. In the later anodic process, the weak oxidation peak at 1.74 V represents the incomplete oxidation of Mo, and the strong oxidation
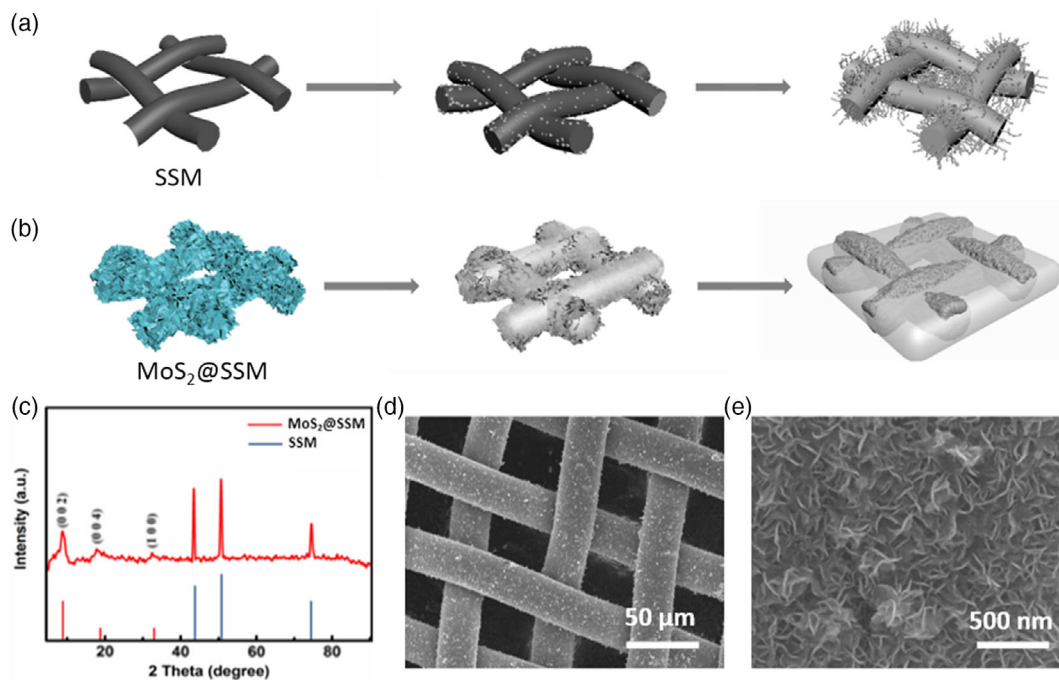
Figure 1. a,b) Schematic illustration of Li deposition on pristine SSM and MoS_2@SSM. c) XRD patterns of MoS_2@SSM. d,e) SEM images of MoS_2@SSM at different magnifications.

**ADVANCED
SCIENCE NEWS**

www.advancedsciencenews.com

**ADVANCED
ENERGY & SUSTAINABILITY
RESEARCH**
Open Access

www.advenergysustres.com

Figure 2. a) CV of the cell with MoS_2@SSM within the voltage window of 0.01–3 V at a scan rate of 0.01 V s^{-1}. b) XPS spectra of MoS_2@SSM before and after discharge to 0.01 V. c–f) High-resolution XPS spectra of c) Mo, e) S before, d) Mo, and f) S after discharge to 0.01 V.

peak at 2.4 V represents the formation of MoS_2. In the second cathodic process, a new reduction peak at 1.5 V was associated with the formation of Li_2S. After the initial conversion reaction, the nanosheet structure of MoS_2 transformed into the porous nanochannel structure of Li_2S/Mo (Figure S4, Supporting Information).

The X-ray photoelectron spectroscopy (XPS) spectra of Mo and S elements were obtained before and after discharge to 0.01 V (Figure 2b-f). As shown in Figure 2c, the peaks at 228.6 and 232.4 eV in the pristine sample before discharge correspond to Mo $3d_{5/2}$ and $3d_{3/2}$ peaks of Mo^{4+} in MoS_2. The small peak at 235.6 eV is ascribed to $3d_{3/2}$ of Mo^{6+} due to surface oxidation. After deconvoluting the two major peaks of Mo^{4+}, the as-synthesized MoS_2 is identified containing both 1 T phase and 2 H phase. The peak at 226.1 eV is S $2s$ characteristic peak.[36,37] In Figure 2e, the peaks at 161.3 and 163 eV are ascribed to S $2p_{3/2}$ and S $2p_{1/2}$ for S^{2-}, respectively. After discharge to 0.01 V, the peaks of Mo $3d_{5/2}$ and $3d_{3/2}$ shift to 232.1 and 235.2 eV, indicating the phase transformation to 3 R phase (Figure 2d). The peaks at 162.63 and 168.2 eV in Figure 2f correspond to S $2p_{3/2}$ and $2p_{1/2}$ in Li_xMoS_2. The XPS results show that the conversion reaction takes place at the Li/MoS_2 interface after discharge to 0.01 V.

Before the nucleation of Li, the preintercalation and conversion of MoS_2 to 0.01 V at constant voltage were conducted, and the kinetics of the preintercalation reaction of the MoS_2@SSM electrode was analyzed by electrochemical impedance spectroscopy (EIS). In Figure S5, Supporting Information, it can be observed that the slope of the straight-line region increases, and the corresponding diffusion impedance decreases after discharge to 0.01 V, which is due the high ionic conductivity of the discharge product Li_2S. After discharging the MoS_2/SSM substrate

to 0.01 V at higher current densities, the diameters of the semicircle in the high-frequency region increased and the linear slope in the low-frequency region also increased (Figure S6, Supporting Information). It can be explained that the formation of additional Li_2S with high ionic conductivity at low current density is beneficial to the diffusion of Li ions.

The migration number of Li ion can be used to characterize the Li-ion diffusion kinetic in the electrolyte, and its value reflects the concentration gradient of Li ion in the electrolyte. The constant voltage chronopotentiometry was used to measure the steady-state current and R_{ct} under the constant voltage condition. By calculating $t_{(SSM)} = 0.3006$ and $t_{(Li2S/Mo@SSM)} = 0.3649$ (Figure S7, Supporting Information), the number of Li-ion migrations increased. The Li-ion conductivity of the Li_2S/Mo arrays was evaluated by EIS. MoS_2@SSM showed a lower resistance compared with SSM. The calculation analysis showed that the Li-ion conductivity of MoS_2@SSM was 6.24×10^{-5} S cm^{-1}, which is higher than that of SSM at 3.94×10^{-5} S cm^{-1} (Figure S8, Supporting Information). The plating of Li ion occurs at the interface between pristine SSM and the electrolyte, resulting in the decrease in ion mobility; the inhomogeneous distribution of the internal electric field contributes to the nucleation of lithium dendrites and the accumulation of charges at the nucleation site, which is the center of further deposition of Li ion, limiting the migration of Li ion. In contrast, the surface electric field of the MoS_2@SSM electrode is evenly distributed, which can be attributed to the increase in the mobility of Li ion.

Before a large amount of Li deposition, the electrode realized Li storage in the Li_2S/Mo grain boundary area at the same time to regulate the deposition of Li.[38] Li prestored in the grain boundary area ensured that the concentration of Li ion at the interface

during the migration process was not zero, which enhanced the ionic conductivity of Li ion and inhibited the growth of Li dendrites. The existence of Mo atoms also guarantees the stability of the array structure. This conclusion can also be matched by Sand's model. When the ion mobility increases, the time τ increases.[11] This can effectively delay the growth of dendrite, maintain high Li-ion flux at the interface of electrode and electrolyte, reduce the concentration gradient of Li ion in the electrolyte, ensure uniform lithium deposition, and further guarantee the excellent electrochemical performance.

The growth behaviors of metallic Li on MoS_2@SSM and SSM substrates at different areal capacities were observed by SEM (**Figure 3**). As shown in Figure 3a,e, metallic Li first deposited on Li_2S/Mo-coated stainless steel wires. When the areal capacity increased from 0.2 to 1 mAh cm^{-2}, the pores between stainless steel wires were gradually filled by Li metal, and no dendritic morphology was observed (Figure 3b-d,f-h). Metallic Li is uniformly and completely coated on the surface of MoS_2@SSM electrode, which is in contrast with the deposition behavior of

metallic Li on the pristine SSM substrate (Figure 3i-p). The inhomogeneity of the surface morphology of the SSM electrode results in the uneven distribution of surface current density and the direct generation of Li dendrites during deposition.

In the early process of Li deposition, the initial nucleation behavior will affect the following deposition of Li. If the Li nucleation is uniform, the morphology of Li deposition will be even, which effectively suppress the growth of Li dendrites. When the deposition of metallic Li occurs below 0 V versus Li/Li$^+$, the voltage will rapidly drop to the lowest point, at which Li nucleation takes place and then starts to rise and reach a flat voltage plateau with lower overpotential, corresponding to the continuous Li deposition. The difference between the lowest voltage of the dip at the beginning and the voltage of the following plateau is defined as Na metal nucleation overpotential. The advantage of the MoS_2@SSM electrode has been confirmed by the reduced nucleation potential, as shown in Figure S9a, Supporting Information. The nucleation potential of the MoS_2@SSM electrode at the current density of 1 mA cm^{-2} is much lower than
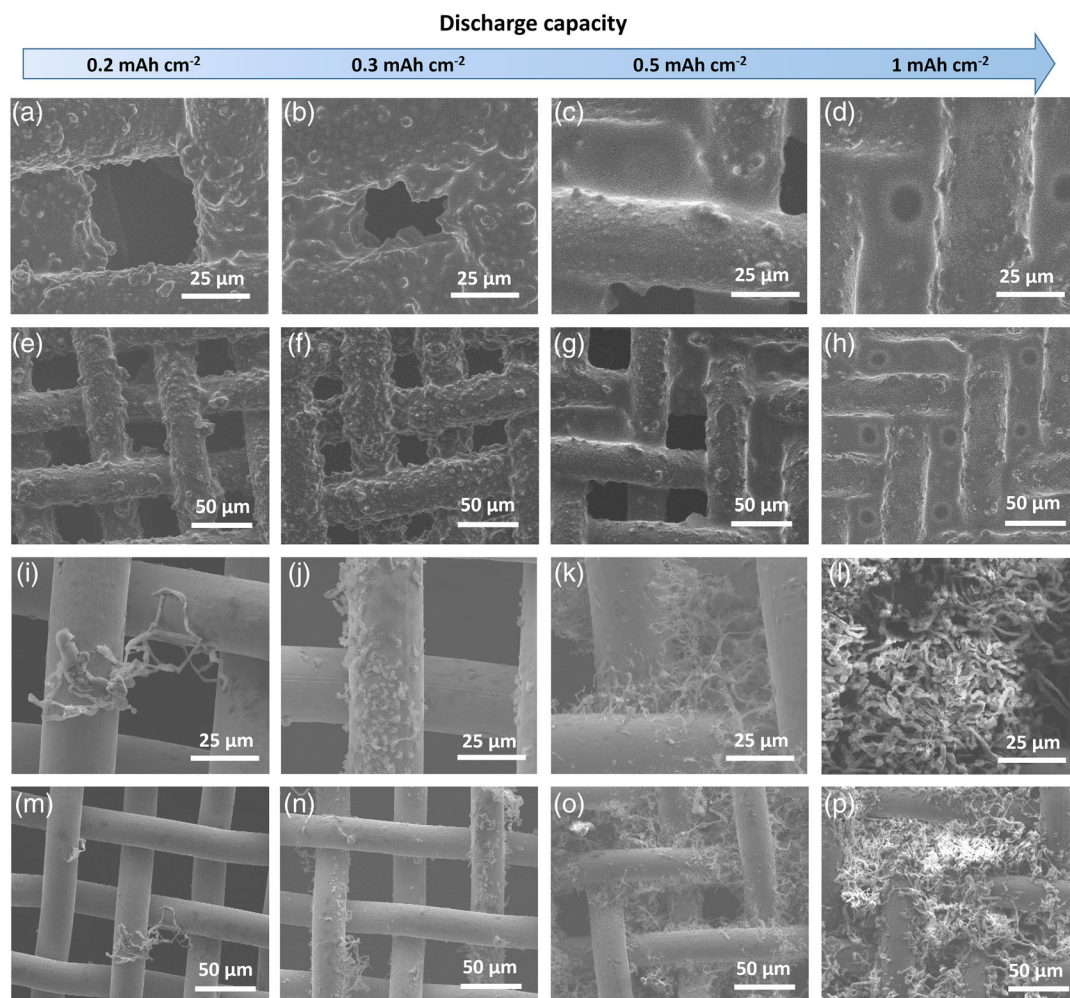

Figure 3. a−h) SEM images of the surface morphology evolution of Li deposition on MoS_2@SSM substrate with the capacity limitation of a,e) 0.2 mAh cm^{-2}, b,f) 0.3 mAh cm^{-2}, c,g) 0.5 mAh cm^{-2}, and d,h) 1 mAh cm^{-2}, respectively. i−p) SEM images of the surface morphology evolution of Li deposition on pristine SSM substrate with the capacity limitations of i,m) 0.2 mAh cm^{-2}, j,n) 0.3 mAh cm^{-2}, k,o) 0.5 mAh cm^{-2}, and i,p) 1 mAh cm^{-2}, respectively.

that of the SSM electrode. The low nucleation potential indicates that MoS$_2$@SSM electrode has excellent lithiophilic property.
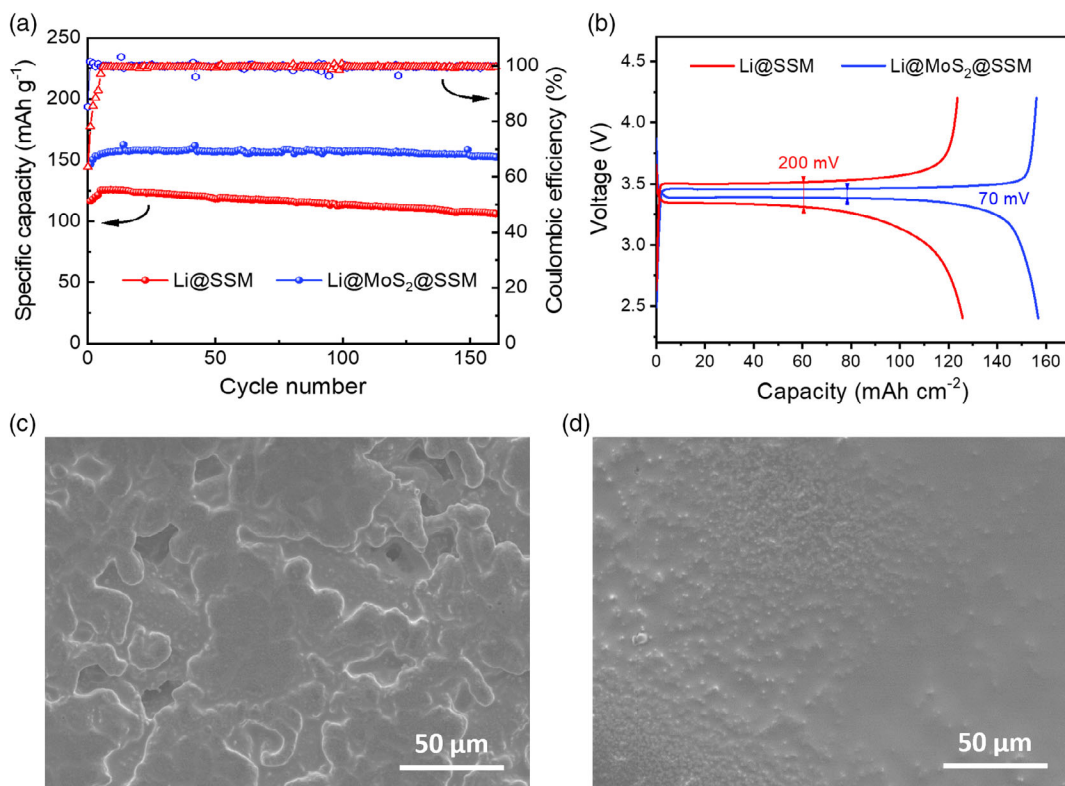
As shown in **Figure 4**a, the cell with MoS$_2$@SSM current collector shows excellent cycling stability at 1 mA cm^{-2} with the capacity limitation of 1 mAh cm^{-2}. The average Coulombic efficiency can remain above 96% for more than 400 cycles. In contrast, the cell with SSM current collector only maintains good stability for about 120 cycles. After that, the Coulombic efficiencies drop sharply. The voltage profiles of the cell with MoS$_2$@SSM current collector show much lower overpotential and higher Coulombic efficiency than that of the cell with SSM current collector at the 125th cycle (Figure S10, Supporting Information). The cycle stability of the half-cell can also be confirmed by the voltage−time curve. Under the testing conditions at 1 mA cm^{-2} and 1 mAh cm^{-2}, the cell with MoS$_2$@SSM current collector exhibited a long cycle stability of more than 450 h, whereas the voltage of SSM electrode fluctuated greatly, resulting in short circuit after 250 h (Figure S11, Supporting Information). This is because Li deposited directly on the SSM fibers, resulting in uneven deposition and dendrite

formation. A large amount of Li was continuously consumed due to the formation of SEI. The decrease in Coulombic efficiency and random unrestrained growth of dendrites punctured the membrane, resulting in short circuiting in the cell. These results further indicate that the unique structure of Li$_2$S/Mo interlayer with both electronic conductivity and ionic conductivity is beneficial for the regulation of homogeneous Li-ion deposition behavior.

Figure S12, Supporting Information, shows the impedance spectrum of the cells with pristine SSM and MoS$_2$@SSM substrates after cycling for different cycles under the conditions of 1 mA cm^{-2} and 1 mAh cm^{-2}. The Nyquist plot is a half arc at the high frequency, which corresponds to the electrochemical load transfer resistance in the process of electrode reaction. A diagonal of the Nyquist plots at the low frequency corresponds to the diffusion resistance of Li ion in the electrode. The deposition/dissolution processes on MoS$_2$@SSM substrates are controlled by electrochemical charge transfer and Li-ion diffusion. R_{ct} of the bare SSM anode decreased significantly with the increase in cycle times, which was due to the formation of dendrites
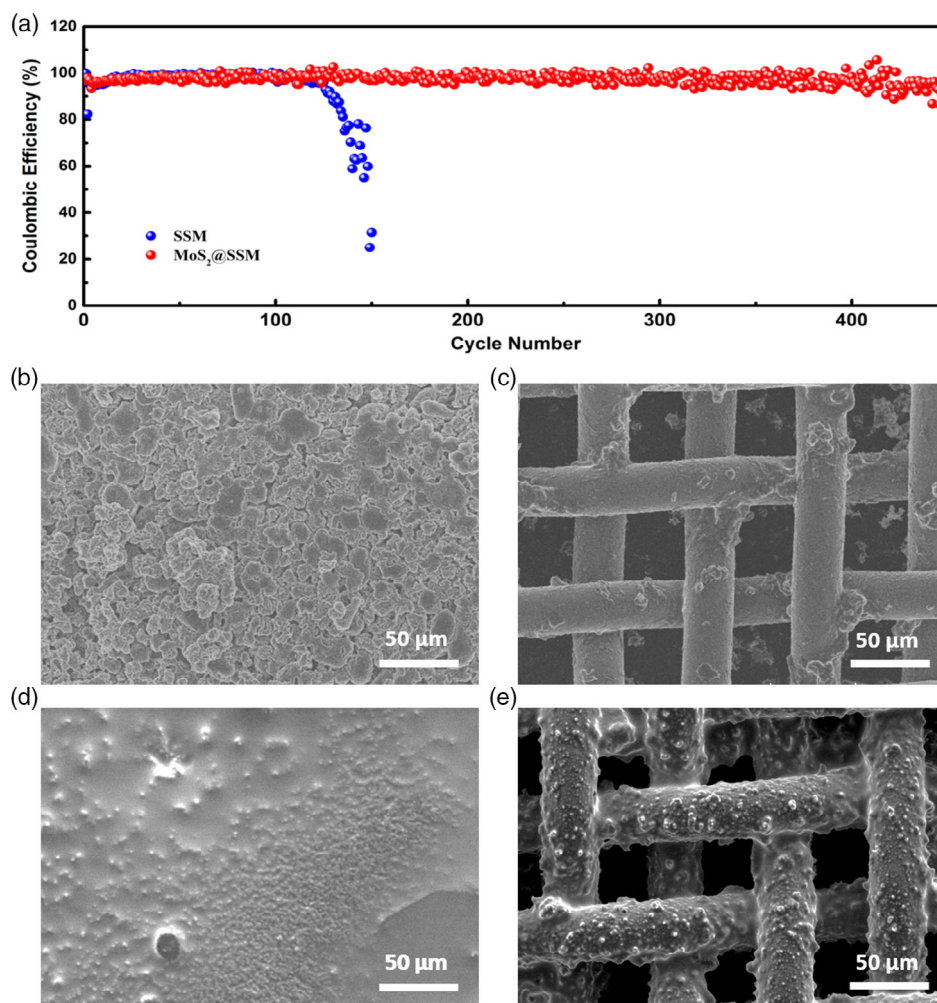
Figure 4. The Coulombic efficiencies of Li plating and stripping on SSM and MoS$_2$@SSM substrates at the areal capacity of 1 mAh cm^{-2} and the current density of 1 mA cm^{-2}. b,c) SEM images of SSM electrodes after 150 cycles: b) plating and c) stripping. d,e) SEM images of MoS$_2$@SSM electrodes after 300 cycles: d) plating and e) stripping.

**ADVANCED
SCIENCE NEWS**

www.advancedsciencenews.com

**ADVANCED
ENERGY & SUSTAINABILITY
RESEARCH**
Open Access

www.advenergysustres.com

Figure 5. a) The cycling performance and Coulombic efficiencies of LFP ∥ Li@SSM full cell and LFP ∥ Li@MoS$_2$@SSM full cell at 1 C. b) The corresponding charge−discharge voltage versus capacity profiles at the tenth cycle. The surface morphology of c) Li@SSM anode and d) Li@MoS$_2$@SSM anode after 150 cycles.

on the surface, the increase in specific surface area, and the irregular process of Li ions being reduced to Li. In contrast, the change of R_{ct} of MoS$_2$@SSM anode is much smaller, indicating the homogeneous Li deposition and stable SEI.

The morphology changes of Li deposition under cycling were investigated by SEM. After 150 cycles at 1 mA cm^{-2} and 1 mAh cm^{-2}, Li deposition on the surface of the SSM electrode presents an inhomogeneous morphology. A large number of "dead Li" was found after Li stripped, which is due to the incomplete Li plating/stripping during many charge−discharge processes. The Coulombic efficiency is under 100% and the active Li cannot be fully utilized—the repetition stacked on the surface. However, after 300 cycles of MoS$_2$@SSM electrodes, it can be observed that the surface coating is still uniform without obvious Li dendrites. Therefore, the morphology of SSM modified by MoS$_2$ after repeated cycling showed that the transformation of MoS$_2$ into Li$_2$S/Mo could provide a lithiophilic interface and a high ionic conductor with uniform Li-ion flux, which improves the electrochemical performance.

For practical application, the commercial cathode material, LiFePO$_4$ (LFP), is selected as the cathode to assemble the full cell. First, 15 mAh cm^{-2} of metallic Li was predeposited on SSM or MoS$_2$@SSM substrates at a current density of 1 mA cm^{-2} to form Li@SSM and Li@MoS$_2$@SSM anodes. **Figure 5**a,b shows the tenth charge/discharge curve of two full cells at 1 C. LFP ∥ Li@MoS$_2$@SSM cell shows a flat voltage platform with lower voltage polarization (70 mV). In addition, the EIS test

(Figure S13, Supporting Information) further confirmed the excellent performance of LFP ∥ Li@MoS$_2$@SSM cell in terms of dynamics, with lower charge transfer resistance and ion diffusion resistance, which indicated that the ion diffusion was improved. Due to the stability and high ionic conductivity of Li$_2$S/Mo interlayer, the surface-modified SSM electrode showed improved electrochemical performance. After a long-term cycle at 1 C, the surface morphology of the two electrodes is shown in Figure 5c,d. There are a large number of lithium dendrites on the surface of the Li@SSM electrode, which may cause short circuit by piercing the separator. In contrast, the surface of the Li@MoS$_2$@SSM electrode is smooth and flat, without obvious Li dendrites and "dead Li."

3. Conclusion

In summary, MoS$_2$ nanosheets were fabricated on SSM substrates by a simple one-step hydrothermal method. The highly ionic-conductive Li$_2$S generated via in situ conversion reaction from MoS$_2$ significantly improved Li-ion transportation kinetics and uniform Li-ion flux, which promoted homogeneous lithium nucleation and deposition. Using MoS$_2$@SSM as substrate for Li-metal anodes in both symmetrical cells and full cells could significantly improve the cycling stability and Coulombic efficiency. This work provides a new strategy using metal sulfides to regulate homogeneous lithium nucleation and inhibit dendritic growth in lithium metal anode.

**ADVANCED
SCIENCE NEWS**

www.advancedsciencenews.com

**ADVANCED
ENERGY & SUSTAINABILITY
RESEARCH**

www.advenergysustres.com

4. Experimental Section

Materials: Sodium molybdate (Na$_2$MoO$_4$·2H$_2$O, Sinopharm Chemical Reagent Co., Ltd, China, 98%), L-cysteine (C$_3$H$_7$NO$_2$S, Shanghai Sigma Aldrich co., Ltd, China, 99%), sodium borohydride (NaBH$_4$, Sinopharm Chemical Reagent Co., Ltd, China), and N,N-dimethylformamide (DMF, Shanghai Sigma Aldrich co., Ltd, China, 99%) were directly used without further purification. The SSM was washed with deionized water and ethanol three times.

Sample Preparation: MoS$_2$ nanosheet arrays grown in situ on SSM were prepared by the one-pot solvothermal method. Na$_2$MoO$_4$·2H$_2$O (96 mg) used as the molybdenum source, C$_3$H$_7$NO$_2$S (152 mg) used as the sulfur source, and NaBH$_4$ (56 mg) used as the reducing agent were added in 70 mL H$_2$O/DMF mixed solvent (volume ratio: 1.5:1) and stirred for 30 min. Then, the mixed solution was transferred to a 100 mL Taflon-lined stainless autoclave. Subsequently, the autoclave was sealed and heated at 200 °C for 12 h. After the autoclave cooled down to room temperature naturally, the obtained MoS$_2$-coated SSM was taken out and washed with distilled water three times. The final MoS$_2$@SSM substrates were obtained after being fully dried at 60 °C for 12 h under vacuum.

Materials Characterization: X-ray diffraction (PANalytical X'Pert PRO, monochromated Cu Kα radiation 40 mA, 40 kV) was used to confirm the crystal structure of obtained materials. XPS analysis was used to analyze the compositions and content of elements. The energy resolution was 0.5 eV and the step size was 0.1 eV. A scanning electron microscope (Hitachi, SU8010) was utilized to characterize the microstructure of the samples.

Electrochemical Measurements: The SSM or MoS$_2$@SSM substrate was used as the working electrode without additional conductive additive and insulting binder. CR2025-type coin cells were assembled in a glovebox filled with high-purity Ar, using lithium metal plates as the counterelectrodes and Celgard 2400 membranes as the separators. The ether-based electrolyte of 1 M lithium bis (trifluoromethanesulfonyl) imide (LiTFSI) in 1, 3-dioxolane (DOL) and dimethoxymethane (DME) (1:1 by volume) with 2 wt% LiNO$_3$ as additive was utilized. During each galvanostatic cycle, the cutoff voltage of 0.5 V was set for the lithium-stripping process.

The full cells were assembled using LiFePO$_4$ as the cathode material. Controlled Li metal anodes were prepared by depositing 15 mAh cm^{-2} of Li on the SSM substrates or MoS$_2$@SSM substrates at the current density of 1 mA cm^{-2}. The galvanostatic charge–discharge tests were conducted at different current densities with a cutoff voltage range from 2.4 to 4.2 V. The cycling performances were tested by a NEWARE BTS-610 (NEWARE Co. Ltd, China) battery tester. The EIS of the coin cells were measured on a CHI660E workstation, and the frequency range was from 1 MHz to 1 Hz. The CV measurement was also recorded with CHI660D workstation from 0.01 to 3.0 V versus Li/Li$^+$ at a scan rate of 0.1 V s^{-1}.

The migration numbers of lithium ion (Li$^+$) were calculated by constant voltage chronopotentiometry measurement and Nyquist plots under the constant voltage condition. The specific numbers can be calculated by the following equation.

$$t_{Li^+} = \frac{I_S(V - I_0 R_0)}{I_0(V - I_S R_S)}$$ (1)

where t_{Li^+} is the migration numbers; I_o and I_s represent the initial transient-state and steady-state current; R_o and R_s refer to the initial transient-state and steady-state resistances of the electrodes; and V is a constant polarization potential of 10 mV.

The ionic conductivity of SSM and MoS$_2$@SSM electrodes was measured by Nyquist plots with CHI660d electrochemistry workstation. In a cell, a separator wet with electrolyte was placed between the stainless steel electrode and SSM or MoS$_2$@SSM substrate. The ionic conductivity was calculated according to the following equation.

$$\sigma = \frac{l}{AR}$$ (2)

where σ represents Li$^+$ conductivity, l is the thickness of the electrode, A the area of the prepared electrode, and R refers to the bulk resistance.

Supporting Information

Supporting Information is available from the Wiley Online Library or from the author.

Conflict of Interest

The authors declare no conflict of interest.

Data Availability Statement

Research data are not shared.

[1] Y. Yao, Z. Wei, H. Wang, H. Huang, Y. Jiang, X. Wu, X. Yao, Z. S. Wu, Y. Yu, *Adv. Energy Mater.* **2020**, *10*, 1903698.

[2] R. Xu, Y. Yao, H. Wang, Y. Yuan, J. Wang, H. Yang, Y. Jiang, P. Shi, X. Wu, Z. Peng, *Adv. Mater.* **2020**, *32*, 2003879.

[3] H. Shi, Y. Dong, S. Zheng, C. Dong, Z.-S. Wu, *Nanoscale Adv.* **2020**, *2*, 4212.

[4] H. Shi, M. Yue, C. J. Zhang, Y. Dong, P. Lu, S. Zheng, H. Huang, J. Chen, P. Wen, Z. Xu, *ACS nano* **2020**, *14*, 8678.

[5] M. Gao, H. Li, L. Xu, Q. Xue, X. Wang, Y. Bai, C. Wu, *J. Energy Chem.* **2021**, *59*, 666.

[6] L. Fan, H. Wu, X. Wu, M. Wang, J. Cheng, N. Zhang, Y. Feng, K. Sun, *Electrochim. Acta* **2019**, *295*, 444.

[7] H. Shi, X. Ren, J. Lu, C. Dong, C. Liu, Q. Yang, J. Chen, Z. S. Wu, *Adv. Mater.* **2020**, *10*, 2002271.

[8] Y. Boyjoo, H. Shi, E. Olsson, Q. Cai, Z. S. Wu, J. Liu, G. Q. Lu, *Adv. Mater.* **2020**, *10*, 2000651.

[9] R. Zhang, X.-R. Chen, X. Chen, X.-B. Cheng, X.-Q. Zhang, C. Yan, Q. Zhang, *Angew. Chem., Int. Ed.* **2017**, *56*, 7764.

[10] X.-B. Cheng, R. Zhang, C.-Z. Zhao, Q. Zhang, *Chem. Rev.* **2017**, *117*, 10403.

[11] D. Lin, Y. Liu, Y. Cui, *Nat. Nanotechnol.* **2017**, *12*, 194.

[12] Q. Xu, X. Yang, M. Rao, D. Lin, K. Yan, R. Du, J. Xu, Y. Zhang, D. Ye, S. Yang, *Energy Storage Mater.* **2020**, *26*, 73.

[13] E. C. Evarts, *Nature* **2015**, *526*, S93.

[14] J. Chen, Q. Li, T. P. Pollard, X. Fan, O. Borodin, C. Wang, *Mater. Today* **2020**, *39*, 118.

[15] L. Xiao, Z. Zeng, X. Liu, Y. Fang, X. Jiang, Y. Shao, L. Zhuang, X. Ai, H. Yang, Y. Cao, *ACS Energy Lett.* **2019**, *4*, 483.

[16] S. Liu, Q. Zhang, X. Wang, M. Xu, W. Li, B. L. Lucht, *ACS Appl. Mater. Interfaces* **2020**, *12*, 33719.

[17] L. Lin, J. Wang, R. Li, C. Wang, C. Zhang, J. Yang, Y. Qian, *Energy Storage Mater.* **2020**, *26*, 112.

[18] J. Liang, Q. Chen, X. Liao, P. Yao, B. Zhu, G. Lv, X. Wang, X. Chen, J. Zhu, *Angew. Chem., Int. Ed.* **2020**, *59*, 6561.

[19] P. Shi, T. Li, R. Zhang, X. Shen, X. B. Cheng, R. Xu, J. Q. Huang, X. R. Chen, H. Liu, Q. Zhang, *Adv. Mater.* **2019**, *31*, 1807131.

[20] H. Shi, J. Qin, K. Huang, P. Lu, C. Zhang, Y. Dong, M. Ye, Z. Liu, Z. S. Wu, *Angew. Chem., Int. Ed.* **2020**, *59*, 12147.

[21] Q. Cheng, A. Li, N. Li, S. Li, A. Zangiabadi, W. Huang, A. C. Li, T. Jin, Q. Song, W. Xu, *Joule* **2019**, *3*, 1510.

[22] X.-B. Cheng, C.-Z. Zhao, Y.-X. Yao, H. Liu, Q. Zhang, *Chem* **2019**, *5*, 74.

[23] F. Zhao, Q. Sun, C. Yu, S. Zhang, K. Adair, S. Wang, Y. Liu, Y. Zhao, J. Liang, C. Wang, *ACS Energy Lett.* **2020**, *5*, 1035.

[24] W. Wu, J. Duan, J. Wen, Y. Chen, X. Liu, L. Huang, Z. Wang, S. Deng, Y. Huang, W. Luo, *Sci. China Chem.* **2020**, *63*, 1483.

[25] S. Tang, X. Zhang, Y. Li, J. Tian, Y. Zhao, L. Mai, L. Wang, Y.-C. Cao, W. Zhang, *J. Alloys Compd.* **2020**, *843*, 155839.

[26] Z. Tu, S. Choudhury, M. J. Zachman, S. Wei, K. Zhang, L. F. Kourkoutis, L. A. Archer, *Nat. Energy* **2018**, *3*, 310.

[27] M. Li, X. Liu, Q. Li, Z. Jin, W. Wang, A. Wang, Y. Huang, Y. Yang, *J. Energy Chem.* **2020**, *41*, 27.

[28] Y. Liu, X. Qin, S. Zhang, L. Zhang, F. Kang, G. Chen, X. Duan, B. Li, *J. Mater. Chem. A* **2019**, *7*, 13225.

[29] H. Duan, J. Zhang, X. Chen, X.-D. Zhang, J.-Y. Li, L.-B. Huang, X. Zhang, J.-L. Shi, Y.-X. Yin, Q. Zhang, *J. Am. Chem. Soc.* **2018**, *140*, 18051.

[30] Y. Shi, Z. Wang, H. Gao, J. Niu, W. Ma, J. Qin, Z. Peng, Z. Zhang, *J. Mater. Chem. A* **2019**, *7*, 1092.

[31] Y. L. Haodong Shi, Lu Pengfei, Wu Zhong-Shuai, *Acta Phys. Chim. Sin.* **2021**, *37*, 2008033.

[32] J. Duan, Y. Zheng, W. Luo, W. Wu, T. Wang, Y. Xie, S. Li, J. Li, Y. Huang, *Nat Sci. Rev.* **2020**, *7*, 1208.

[33] G. Huang, P. Lou, G.-H. Xu, X. Zhang, J. Liang, H. Liu, C. Liu, S. Tang, Y.-C. Cao, S. Cheng, *J. Alloys Compd.* **2020**, *817*, 152753.

[34] G. Huang, S. Chen, P. Guo, R. Tao, K. Jie, B. Liu, X. Zhang, J. Liang, Y.-C. Cao, *Chem. Eng. J.* **2020**, *395*, 125122.

[35] K. Chang, D. Geng, X. Li, J. Yang, Y. Tang, M. Cai, R. Li, X. Sun, *Adv. Mater.* **2013**, *3*, 839.

[36] F. Chen, D. Shi, M. Yang, H. Jiang, Y. Shao, S. Wang, B. Zhang, J. Shen, Y. Wu, X. Hao, *Adv. Funct. Mater.* **2021**, *31*, 2007132.

[37] M. Wu, J. Zhan, K. Wu, Z. Li, L. Wang, B. Geng, L. Wang, D. Pan, *J. Mater. Chem. A* **2017**, *5*, 14061.

[38] S. Xia, Y. Wang, Y. Liu, C. Wu, M. Wu, H. Zhang, *Chem. Eng. J.* **2018**, *332*, 431.